Combining dual-tree wavelet analysis and proximal optimization for anisotropic scalefree texture segmentation

Leo Davy, Nelly Pustelnik, Patrice Abry

COMBINING DUAL-TREE WAVELET ANALYSIS AND PROXIMAL OPTIMIZATION FOR ANISOTROPIC SCALEFREE TEXTURE SEGMENTATION

Leo Davy, Nelly Pustelnik, Patrice Abry

CNRS, Ecole Normale Supérieure de Lyon, Laboratoire de physique, Lyon, France
firstname.lastname@ens-lyon.fr

ABSTRACT

The present work addresses the segmentation of textures characterized by anisotropy and scalefree statistics, two generic properties of use to model numerous real-world applications. This is achieved by proposing to combine a complex dualtree multiscale (wavelet) analysis within an inverse problem formulation aiming to estimate anisotropy and scalefree local parameters and to group them into piecewise homogeneous patches, jointly and in one single step. To minimize the corresponding functional, a primal-dual proximal convergent algorithm is devised and accelerated by taking advantage of the strong convexity of the data-fidelity term. Segmentation performance are assessed as function of the complexity of the task by means of Monte Carlo simulations conducted over synthetic textures, defined from anisotropic scalefree stochastic models.

***Index Terms*—** Anisotropy, scalefree, texture, dual-tree, total-variation, proximal algorithms, strong convexity.

1. INTRODUCTION

Context. Texture segmentation constitutes a canonical task in Image processing, ubiquitous in applications, that raised tremendous amounts of researches along many different scientific lines (cf. e.g., [1, 2, 3, 4, 5, 6]). Also, a large variety of texture models were proposed attempting to account for generic statistical properties (cf. e.g., [7] for a review). In the present work, the relevance of a nonsmooth convex proximal-based minimization is investigated, for the segmentation of textures characterized by both anisotropy and scalefree dynamics, two generic statistical features relevant in many different applications (cf. e.g., [8, 9, 10, 11, 11, 12, 13]).

Related works. Image segmentation often relies on exploiting geometry. Stochastic texture segmentation thus can be regarded as a more challenging task, as they essentially have no geometry and are characterized by their statistical properties only. Texture segmentation is commonly based on two-step approaches: extraction/estimation of descriptors/features followed by segmentation. Several research lines ranging from Non Negative Matrix Factorization [4] to deep learning [14] have significantly contributed to revisiting this two-step approach by combining into a single step this feature estimation and segmentation. The main limitation of supervised segmentation relies though on the need to use (usually large) training datasets, as well as on large computing and storage capabilities. Moreover, such large databases are often not available because expert annotations may be too costly or even not feasible. Therefore, despite the massive potential of (deep) learning, contexts where large documented databases are not available, where boundary estimation accuracy is of primer importance to the application, and where understanding the role of the features is as important as segmentation performance, unsupervised segmentation strategies remain of critical importance. In that spirit, in [15, 6], a one step stochastic texture segmentation procedure was proposed, combining fractal feature estimation and segmentation, formulated as a penalized least square minimization problem. However, its extension to segmentation based jointly on local scalefree and anisotropy features remains an open question, addressed here.

Goals, contributions and outline. The present work proposes an original texture segmentation formulation that combines, in a single step, the estimation of anisotropic-scalefree local features, and their grouping into piecewise homogeneous patches, solved with appropriate proximal minimization procedure. To that end, Section 2 details, first, the class of Gaussian stochastic processes used as models for anisotropic scalefree textures, second, a directional multiband multiscale (dual-tree complex wavelet) analysis, and proposes, as a first contribution, the estimation, for such textures, of *global* anisotropic-scalefree features from dual-tree coefficients. In Section 3, as main contribution of this work, we propose a penalized least squares minimization problem, that performs in a single step a piecewise constant estimation of *local* anisotropic-scalefree features, thus permitting an efficient a posteriori segmentation of textures. Three variations of the corresponding functional are detailed depending on the nature of the anisotropy. Section 4 develops an accurate and efficient algorithm based on proximal operator theory to minimize the corresponding functional. It is also shown how to exploit explicitly the strong convexity of the data-fidelity term for convergence acceleration. Finally, Section 5 reports achieved segmentation performance, assessed by Monte Carlo simulations conducted over synthetic prescribed piecewise homogeneous anisotropic scalefree textures. It shows the benefits of involving anisotropic (as opposed to isotropic only) local features for segmentation.

2. HOMOGENEOUS ANISOTROPIC SCALEFREE TEXTURES: MODELS AND ANALYSIS

Anisotropic scalefree Models. Gaussian random fields were classically used to model textures, especially through variations of the Brownian fields [16, 17, 18, 19, 20]. Following this line, the Gaussian field used in this work, denoted $X : \mathbb{R}^2 \to \mathbb{R}$, is here defined via its power spectral density (PSD) f, with $\mathrm{x} = (x, y)$ and $\widehat{W}$ the Fourier transform of a Gaussian white noise:

$$(\forall \mathrm{x} \in \mathbb{R}^2) \quad X^f(\mathrm{x}) = \int_{\mathbb{R}^2} (e^{i\langle \mathrm{x}, \xi \rangle} - 1) \sqrt{f(\xi)} \widehat{W} \, \mathrm{d}\xi. \qquad (1)$$

To incorporate both anisotropy and scalefree (selfsimilarity) spatial dynamics in separable and controllable manners, it has been con-

This work is supported by the ANR (Agence Nationale de la Recherche) from France ANR-19-CE48-0009 Multisc'In.

sidered in [16, 21] that the PSD f is written as:

$$f(\xi) = \tau\left(\frac{\xi}{||\xi||}\right)||\xi||^{-2h\left(\frac{\xi}{||\xi||}\right)-2}, \quad (2)$$

with *topothesis function* $\tau : \mathbb{S}_1 \to \mathbb{R}_+$ and *Hurst function* $h : \mathbb{S}_1 \to [0, 1]$ chosen as angular functions where $\mathbb{S}_1$ is the unit circle in $\mathbb{R}^2$. The resulting Gaussian field X^f is referred to as *Anisotropic Fractional Brownian Field* (AFBF).

We are focusing here on several configurations of AFBF:

- When both τ and h are constant functions, $\tau(\xi) \equiv \sigma^2$ and $h(\xi) \equiv H$, X^f simplifies to an isotropic selfsimilar field with self-similarity exponent H, referred to as fractional Brownian field (H-FBF) (Fig. 1 left).
- When $h(\xi) \equiv H$ but τ depends on ξ, X^f remains exactly self-similar but with anisotropy (H-AFBF) (Fig. 1 middle left).
- When $h(\xi)$ depends on ξ, with $\tau(\xi) \equiv \sigma^2$, exact selfsimilarity is lost and the scale free property is weakened into an asymptotic property in the limit of high frequencies (or fine scales) (Fig. 1 middle right).
- When both h and τ depend on ξ, scalefree dynamics is only asymptotic and anisotropy is complicated as it stems from two different and independent mechanisms, (Fig. 1 right).

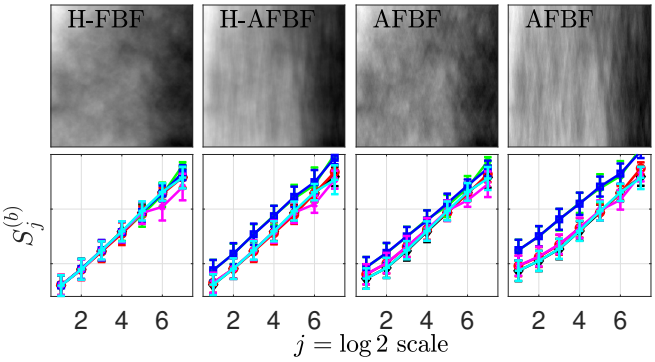

Fig. 1. **Anisotropic Fractional Brownian Fields (AFBF).** Top: Examples of homogeneous textures X^f. Bottom: Function $S_j^{(b)} \equiv \sum_k \log_2 |d_{j,k}^{(b)}|^2$ (with $d_{j,k}^{(b)}$ dual-tree complex wavelet coefficient at scale 2^j, location k and band b) where each color corresponds to a different value of b. From left to right, textures are globally isotropic selfsimilar, anisotropic selfsimilar, anisotropic asymptotically selfsimilar (with anisotropy induced by h only), anisotropic asymptotically selfsimilar.

Multiscale multiband wavelet analysis. It has been abundantly documented that scalefree dynamics in time series and isotropic textures can be efficiently analyzed by means of multiscale (wavelet) transforms [22]. For anisotropic textures, the use of complex and direction-sensitive dependent wavelet transforms must be used, amongst which the elegant and efficient dual-tree complex wavelet decomposition is considered the state-of-the-art [23, 24, 25], thus used here and briefly recalled below.

From a classical pair of univariate scaling function ϕ_h and wavelet ψ_h [26] and from their Hilbert transform $\psi_g = \mathcal{H}(\psi_h)$ and $\phi_g = \mathcal{H}(\phi_h)$. The dual-tree complex wavelet construction [23] defines a collection of $B = 6$ directional complex wavelets $\{\psi^{(b)}(x)\}$. For each scale 2^j, location x, and band $1 \le b \le B$, the wavelet coefficients

$$d_j^{(b)}(\mathrm{x}) = \langle X^f(\mathrm{x}), 2^{-j/2}\psi^{(b)}(2^{-j}\mathrm{x})\rangle \quad (3)$$

convey directional (hence anisotropic) multiscale information related to the spatial dynamics of texture X^f [23, 24, 25, 27].

Multiband wavelet analysis of homogeneous AFBF. Following classical results in time series and real wavelets, see e.g. [28, 29, 30, 31], it can be shown that the (complex) wavelet coefficients of 2D Gaussian fields (with PSD f) with stationary increments are zero-mean jointly stationary Gaussian processes with variance:

$$\mathbb{E}|d_j^{(b)}(\mathrm{x})|^2 = \int_{\mathbb{R}^2} \tau(\xi)||2^{-j}\xi||_2^{-2(h(\xi)+1)}|\widehat{\psi^{(b)}}(\xi)|^2 2^j \mathrm{d}\xi. \quad (4)$$

Calculations, not reported here but expanding to images and complex wavelets those classically conducted in e.g., [32, 29, 30, 31] for time series and real wavelets, show that the expectation $\mathbb{E}$ of $l_j^{(b)}(\mathrm{x}) \equiv \log_2 |d_j^{(b)}(\mathrm{x})|^2$ follows a linear dependency with respect to the logarithm of the scale, exactly for H-FBF and H-AFBF, and approximately under mild hypothesis on mother-wavelets for AFBF in general:

$$\mathbb{E}l_j^{(b)}(\mathrm{x}) = v^{(b)}(\mathrm{x}) + jh^{(b)}(\mathrm{x}). \quad (5)$$

By Eq. (1), $\mathbb{E}l_j^{(b)}(\mathrm{x})$ does not depend on the location x for homogeneous textures, we can thus perform a global multiscale analysis by replacing ensemble averages $\mathbb{E}$ by spatial averages: $S_j^{(b)} \equiv \sum_{\mathrm{x}} l_j^{(b)}(\mathrm{x})$.

Functions $S_j^{(b)}$, computed from a single observation of the textures displayed in Fig. 1(top row), are reported in Fig. 1(bottom row). Their behaviors as functions of the octave j ($\log_2$ of the scales 2^j) constitutes the multiscale multiband signatures of the anisotropy and scalefree properties of the textures X^f:

- For H-FBF, $v^{(b)}$ and $H^{(b)}$, for $b = 1, \ldots, B$, no longer depend on directions and are thus all equal.
- For H-AFBF, the $v^{(b)}$ depend on directions, hence on b, while the $H^{(b)}$ do not.
- For AFBF in general, both the $v^{(b)}$ and the $H^{(b)}$ depend on directions, hence on b.

In practice, the estimations of the $v^{(b)}$ and the $H^{(b)}$ stems from linear regressions of $S_j^{(b)}$ against j. Such linear regressions can be written as, for each $b = 1, \ldots, B$:

$$(\widehat{v}^{(b)}, \widehat{h}^{(b)}) = \underset{(v,h)\in\mathbb{R}^2}{\operatorname{argmin}} \sum_j (S_j^{(b)} - jh^{(b)} - v^{(b)})^2. \quad (6)$$

3. PIECEWISE HOMOGENEOUS ANISOTROPIC SCALEFREE TEXTURES: MODELS AND ANALYSIS

Piecewise AFBF model. For modelling a wider range of real-world textures, we propose to use piecewise homogeneous textures defined by concatenating L different AFBF textures $(X^{f^\ell})_{\ell=1}^L$ (with respective τ^ℓ and h^ℓ) according to random partitions of L non-overlapping regions, whose union covers the whole support of the image. The choices of different f^ℓ results into textures with piecewise homogeneous scalefree and anistropic statistical properties. Examples of such textures are shown in Fig. 3 for $L = 2$ and several choices of τ^ℓ and h^ℓ. We now focus on discrete texture, with $\Omega = \{1, \ldots, N\}^2$and locations denoted by $\mathrm{k} = (k_1, k_2)$.

Local analysis. The goal is to be able to segment a single observation of such heterogeneous textures into piecewise homogeneous subtextures when both f_ℓ and the partition are unknown. Heterogeneity precludes global analysis. Instead, the intuition is to perform a local (pixel-wise, for each k) joint estimation of $v_{\mathrm{k}}^{(b)}$ and $h_{\mathrm{k}}^{(b)}$ and to group the pixel k into a region where both the $v_{\mathrm{k}}^{(b)}$ and $h_{\mathrm{k}}^{(b)}$ can

be considered identical. To that end, an intuitive idea is to mimick the global estimations by means of linear regressions, as in Eq. (6), into a collection of local linear regressions:

$$(\widehat{\mathrm{v}},\widehat{\mathrm{h}}) = \underset{(\mathrm{v},\mathrm{h})\in\mathbb{R}^{BN^2}\times\mathbb{R}^{BN^2}}{\operatorname{argmin}} \sum_b \sum_j \sum_{\mathrm{k}} (l^{(b)}_{j,\mathrm{k}} - j h^{(b)}_{\mathrm{k}} - v^{(b)}_{\mathrm{k}})^2.$$

However, this would result into high variance estimates, and no relation between the estimates for the different directions b, and thus poor segmentation performance. Therefore, instead of a 2-step procedure, first local estimation, second segmentation, we propose here to perform a 1-step local estimation enforcing i) piecewise constancy of the $v^{(b)}_{\mathrm{k}}$ and $h^{(b)}_{\mathrm{k}}$ through the space, and ii) cooperation between the different directions b.

To enforce piecewise constancy in the local estimates of the anisotropic scalefree features, a spatial horizontal and vertical total variation (ℓ_1-norm penalization) is used. To ensure the colocation of changes to be cooperatively detected by the different bands $b \in \{1,\dots,B\}$, a mixed across space and bands, $\ell_{2,1}$-norm, penalization is involved, thus resulting in the following functional to minimize:

$$\begin{aligned}(\widehat{\mathrm{v}},\widehat{\mathrm{h}}) = &\underset{(\mathrm{v},\mathrm{h})\in\mathbb{R}^{BN^2}\times\mathbb{R}^{BN^2}}{\operatorname{argmin}} \sum_b \sum_j \sum_{\mathrm{k}} (l^{(b)}_{j,\mathrm{k}} - j h^{(b)}_{\mathrm{k}} - v^{(b)}_{\mathrm{k}})^2 \\ &+ \lambda \sum_{\mathrm{k}} \Big(\sum_{\mathrm{b}} |h^{(b)}_{k_1+1,k_2} - h^{(b)}_{k_1,k_2}|^2 + |h^{(b)}_{k_1,k_2+1} - h^{(b)}_{k_1,k_2}|^2 \\ &+ \alpha |v^{(b)}_{k_1+1,k_2} - v^{(b)}_{k_1,k_2}|^2 + \alpha |v^{(b)}_{k_1,k_2+1} - v^{(b)}_{k_1,k_2}|^2 \Big)^{1/2} \end{aligned} \quad (7)$$

For notation and compactness purposes, this is rewritten as:

$$(\widehat{\mathrm{v}},\widehat{\mathrm{h}}) = \underset{(\mathrm{v},\mathrm{h})}{\operatorname{argmin}} \frac{1}{2} \sum_{\mathrm{k}} ||\mathrm{l}_{\mathrm{k}} - A(\mathrm{v}_{\mathrm{k}}^\top, \mathrm{h}_{\mathrm{k}}^\top)^\top||_2^2 + \lambda \|D^\alpha (\mathrm{v}^\top, \mathrm{h}^\top)^\top\|_{2,1} \quad (8)$$

where, for every location k, $\mathrm{l}_{\mathrm{k}} = (l^{(b)}_{j,k})_{j,b}$ and

$$\|D^\alpha (\mathrm{v}^\top, \mathrm{h}^\top)^\top\|_{2,1} = \sum_k \sqrt{||(D\mathrm{h})_{\mathrm{k}}||_2^2 + \alpha ||(D\mathrm{v})_{\mathrm{k}}||_2^2}$$

where $D = (D_1, D_2)$ models the first horizontal and vertical difference applied on each band. Further, Matrix A can take several forms depending on the assumed underlying texture model:

- For H-FBF, assumed anisotropy leads to estimate locally two features, $v_{\mathrm{k}} \equiv v^{(b)}_{\mathrm{k}}$ and $h_{\mathrm{k}} \equiv h^{(b)}_{\mathrm{k}}$ for all b, resulting in a $BJ \times 2$ matrix,

$$A_{\text{iso}} = \begin{bmatrix} \mathbf{1} & \boldsymbol{J} \\ \vdots & \vdots \\ \mathbf{1} & \boldsymbol{J} \end{bmatrix}$$

with J the the number of scales involves in local linear regressions and where $\mathbf{1} = (1,\cdots,1)^\top \in \mathbb{R}^J$ and $\boldsymbol{J} = (1,2,\cdots,J)^\top \in \mathbb{R}^J$. Matrix A_{iso} is reminiscent of one of the state-of-the-art procedure described in [6] based on real wavelet and a single band $B = 1$.

- For H-AFBF, assumed anisotropic selfsimilarity leads to estimate $B+1 = 7$ local features (e.g. $(v^{(b)}_{\mathrm{k}})_{1\le b\le B}$ and $h_{\mathrm{k}} \equiv h^{(b)}_{\mathrm{k}}$) , resulting in a $BJ \times (B+1)$ matrix, (with $\mathbf{0} = (0,\cdots,0)^\top \in \mathbb{R}^J$),

$$A_{\mathrm{h}} = \begin{bmatrix} \mathbf{1} & \mathbf{0} & \dots & \mathbf{0} & \boldsymbol{J} \\ \mathbf{0} & \mathbf{1} & \mathbf{0} & \dots & \boldsymbol{J} \\ \vdots & \vdots & \ddots & & \\ \mathbf{0} & \dots & \mathbf{0} & \mathbf{1} & \boldsymbol{J} \end{bmatrix}$$

- For generic AFBF with anisotropy and asymptotical only self-similarity, $2 \times B = 12$ local features need to be estimated leading to the $BJ \times 2B$ matrix,

$$A_{\text{full}} = \begin{bmatrix} \mathbf{1} & \mathbf{0} & \dots & \mathbf{0} & \boldsymbol{J} & \mathbf{0} & \dots & \dots & \mathbf{0} \\ \mathbf{0} & \mathbf{1} & \mathbf{0} & \dots & \mathbf{0} & \boldsymbol{J} & \mathbf{0} & \dots & \mathbf{0} \\ \vdots & \vdots & & & & & & & \\ \mathbf{0} & \dots & \mathbf{0} & \mathbf{1} & \mathbf{0} & \dots & \dots & \mathbf{0} & \boldsymbol{J} \end{bmatrix}.$$

4. PROXIMAL MINIMIZATION

Proximal minimization algorithm. To solve Problem (8), various proximal strategies could be employed [33]. Notably, fast schemes can be employed by using the fact that the data-fidelity is γ-strongly convex, for some $\gamma > 0$. Hence, we choose to use the primal-dual Chambolle-Pock algorithm [34] with strongly convex acceleration, such that for every iteration $t \ge 0$:

$$\begin{cases} \mathrm{z}_{t+1} &= \operatorname{prox}_{\sigma_t(\lambda||\cdot||_{2,1})^*}(\mathrm{z}_t + \sigma_t \lambda D^{(\alpha)} \tilde{\mathrm{z}}_t) \\ \mathrm{u}_{t+1} &= \operatorname{prox}_{\tau_t F}(\mathrm{u}_t - \tau_t \lambda D^{(\alpha)*} \mathrm{z}_{t+1}) \\ \theta_t &= \frac{1}{\sqrt{1+2\gamma\tau_t}}, \quad \tau_{t+1} = \tau_t \theta_t, \quad \sigma_{t+1} = \sigma_t/\theta_t \\ \tilde{\mathrm{z}}_{t+1} &= \mathrm{z}_{t+1} + \theta(\mathrm{z}_{t+1} - \mathrm{z}_t). \end{cases}$$

where $F = \sum_{\mathrm{k}} \frac{1}{2}||\mathrm{l}_{\mathrm{k}} - A\cdot||_2^2$ and $\mathrm{z}_t = (\mathrm{v}_t^\top, \mathrm{h}_t^\top)^\top$, which is initialized as the solution of the ordinary least squares linear regression. Both proximity operators involved are well known and have closed-form expressions documented in the literature [35].

Lemma 1. *The strong convexity constant of F : $\gamma = \lambda_{min}(A^*A)$, is given by :*

$$\lambda_{min}(A^*_{iso}A_{iso}) = \frac{BR_2 + BR_0 - B\sqrt{(R_2-R_0)^2 + 4R_1^2}}{2}, \quad (9)$$

$$\lambda_{min}(A^*_h A_h) = \frac{BR_2 + R_0 - \sqrt{(BR_2-R_0)^2 + 4BR_1^2}}{2}, \quad (10)$$

$$\lambda_{min}(A^*_{full}A_{full}) = \frac{\lambda_{min}(A^*_{iso}A_{iso})}{B}. \quad (11)$$

with B the number of bands and $R_n = \sum_{j=1}^J j^n$.

Theorem 1. *Let $\sigma_0\tau_0\lambda^2||D_\alpha||^2 < 1$ and γ provided by Lemma 1, then the sequence $(\mathrm{z}_t)_t$ converges to $\widehat{\mathrm{z}}$ where $\widehat{\mathrm{z}}$ minimizes* (8)*. Additionally, $||\mathrm{z}_t - \widehat{\mathrm{z}}|| = \mathcal{O}(1/t^2)$.*

5. PERFORMANCE ASSESSMENT

5.1. Numerical simulation set-up

Simulation set-up. Simulations were conducted in Python. Textures used here, such as those displayed in Figs. 1 and 3, were synthesized using the PyAFBF library, which relies on the (τ, h) parametrization in (2), and are of size 256×256. Estimations are performed using octaves $j = \{1,\dots,J = 7\}$. Chambolle-Pock algorithm is run until stabilisation of the objective function (500 iterations).

Texture parametrization. To produce experiments for which performance assessment is simple to understand and analyze, the functions $\tau(\theta)$ and $h(\theta)$, with $\theta \in [-\pi/2, \pi/2]$, of the homogeneous textures or piecewise homogeneous textures used here are parametrized on the unit angular disk as illustrated in Fig. 2, with two intensity levels ν^+ and ν^-, a center μ, and a width δ. Considered textures are as follows:

Texture 1: $h(\theta) \equiv 0.65$, $\tau(\theta) \equiv 5$

Texture 2: $h(\theta) \equiv 0.7$, $\tau(\theta) \equiv 5$

Texture 3: $h(\theta) \equiv 0.7$, $\tau : \{\mu_\tau = 0, \delta_\tau = \frac{\pi}{4}, \nu^-_\tau = 1, \nu^+_\tau = 20\}$

Texture 4: $h(\theta) \equiv 0.7, \tau : \{\mu_\tau = \frac{\pi}{8}, \delta_\tau = \frac{\pi}{8}, \nu_\tau^- = 1, \nu_\tau^+ = 20\}$
Texture 5(μ): h: $\{\mu_h = \mu, \delta_h = \frac{\pi}{6}, \nu_h^- = 0.5, \nu_h^+ = 0.7\}, \tau(\theta) \equiv 1$
Texture 6: $h : \{\mu_h = 0 \quad , \delta_h = \frac{\pi}{6}, \nu_h^- = 0.5, \nu_h^+ = 0.7\}$, $\tau : \{\mu_\tau = 0, \delta_\tau = \frac{\pi}{4}, \nu_\tau^- = 1, \nu_\tau^+ = 20\}$.

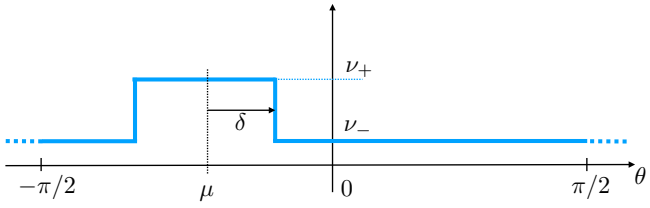

Fig. 2. Parametrization of $\tau(\theta)$ and $h(\theta)$ on the unit disk.

5.2. Local analysis and texture segmentation

Segmentation principle. The local estimates $\widehat{\mathrm{v}}^{(b)}$ and $\widehat{\mathrm{h}}^{(b)}$ obtained from the minimization problem (8) with the algorithm described in Section 4 are concatenated as an array of coordinates for each pixel, to which a standard K-means clustering procedure is applied, with a priori prescribed numbers of clusters (K=2 in our simulations), to yield the final 2-class labeled images.

Visual qualitative assessment. The performance of the proposed texture segmentation procedure are first illustrated visually and qualitatively on four different pedagogical mixtures of piecewise homogeneous textures, with $K = 2$ regions only. The mask used to create these piecewise homogeneous textures is very close to the estimated one displayed in Fig. 3 (bottom right) for which we have almost exact recovery.

Mixture 1 (Texture 1 vs. Texture 2) consists of two isotropic textures with different selfsimilarity parameters h. Fig. 3 (top row) shows that the segmentation obtained with any of the three operator A achieves satisfactory and comparable performance, as indeed, in principle A_{iso} is sufficient to feel the change in texture. Mixture 2 (Texture 3 vs. Texture 4) consists of two H-AFBF with same constant Hurst function h but different functions τ. As expected, A_{iso} fails to achieve segmentation, as it cannot capture anisotropy, while A_{h} and A_{full} perform comparably well, as in principle A_{h} should have enough freedom to feel changes in function τ only. Finally, Mixture 3 (Texture 5 ($\mu = -\frac{\pi}{3}$) vs. Texture 5 ($\mu = -\frac{\pi}{6}$)) and Mixture 4 (Texture 5 ($\mu = -\frac{\pi}{3}$) vs. Texture 5 ($\mu = 0$)) both combine AFBF with changes in h but same τ. As expected, A_{full} only is able to probe anisotropy in a rich enough manner to achieve satisfactory classification.

5.3. Global analysis of homogeneous textures

As illustration, Fig. 1 reports the B functions $S_j^{(b)}$, averaged across 10 realizations for four different homogeneous textures. For H-FBF (left, Texture 2), the B functions $S_j^{(b)}$ collapse one on the other as expected from isotropy. For H-AFBF (middle left, Texture 3), the B functions $S_j^{(b)}$ have same slope but different intercepts. For the two generic AFBF (right plots, Textures 5($\mu = -\frac{\pi}{3}$) and 6), the B functions $S_j^{(b)}$ have different behaviors across scales, as signatures of specific forms of anisotropies.

Quantitative segmentation performance assessment. Segmentation performance are further assessed quantitatively by average over 10 realisations of a mixture between Texture 5 ($\mu = -\frac{\pi}{3}$) and Texture 5 (μ)), consisting of AFBF with functions h that differ in the locations of their centers such that $\Delta\mu_h = -\frac{\pi}{3} - \mu$. For each of the three possible choice of matrix A, performance are computed using a grid of regularization hyperparameters λ. Fig. 4 compares average ($\pm$ standard deviations) error classification as functions of $\Delta\mu_h$, for the λ yielding best performance for each choice of A. Fig. 4 shows that A_{iso} fails to perform any segmentation and that while A_{h} and A_{full} are achieving comparable performance for the mixture with largest differences $\Delta\mu_h \simeq \pi/2$, A_{full} proves to be more robust for a larger range of $\Delta\mu_h$.

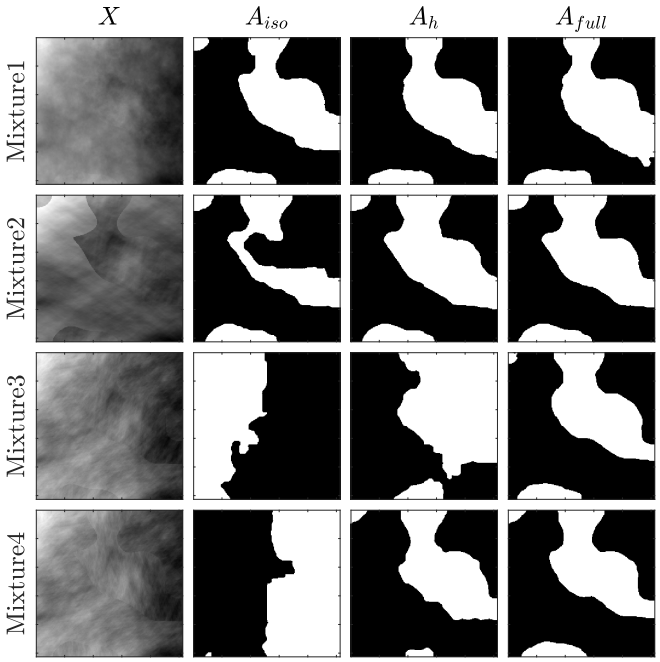

Fig. 3. Texture segmentation of piecewise homogeneous AFBF. Textures X^f (left) and corresponding segmentation using (from left to right) A_{iso}, A_{h} and A_{full} in (8), for four different $K = 2$ mixtures: H-FBF with different H (top), H-AFBF with different τ but same h (2nd row), AFBF with different h but same τ (3rd and bottom rows).

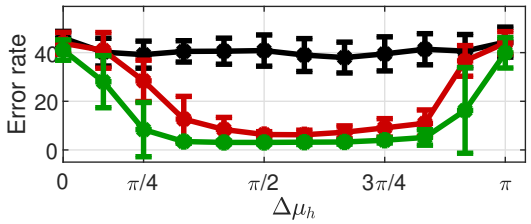

Fig. 4. Segmentation perormance. Percentage of misclassified pixels depending on the rotation angle between hurst functions and choice of regularisation parameter λ. From left to right the model used to obtain segmentations is induced by A_{iso}, A_{h} and A_{full}.

6. CONCLUSIONS AND PERSPECTIVES

Artificial intelligence (AI) and deep neural networks (DNN) constitute natural alternatives against which to compare segmentation performance. However, the design of DNN architectures remains an on-going challenge, involving a competition between always larger computer resources and theoretical foundations. In that perspective, our plans for future investigations are to consider the *unrolling* proximal algorithms, proposed and assessed here, as a means to design an efficient and *frugal* DNN architecture, in an attempt to contribute to sustainable AI, with simpler architectures and smaller training sets.

7. REFERENCES

[1] M. Unser, "Texture classification and segmentation using wavelet frames," *IEEE Trans. Image Process.*, vol. 4, no. 11, pp. 1549–1560, 1995.

[2] M. Jung, G. Peyré, and L. D. Cohen, "Texture Segmentation via Non-local Non-parametric Active Contours," in *Proc. EMMCVPR*, 2011, vol. 6819, pp. 74–88.

[3] A.M. Atto, Y. Berthoumieu, and P. Bolon, "2-Dimensional Wavelet Packet Spectrum for Texture Analysis," *IEEE Trans. Image Process.*, vol. 22, no. 22, pp. 2495 – 2500, June 2013.

[4] J. Yuan, D. Wang, and A. M. Cheriyadat, "Factorization-based texture segmentation," *IEEE Trans. Image Process.*, vol. 24, no. 11, pp. 3488–3497, Nov. 2015.

[5] S. Mikeš and M. Haindl, "Texture segmentation benchmark," *IEEE Trans. Pattern Anal. Match. Int.*, vol. 44, no. 9, pp. 5647–5663, 2021.

[6] B. Pascal, N. Pustelnik, and P. Abry, "Strongly convex optimization for joint fractal feature estimation and texture segmentation," *Appl. Comp. Harm. Analysis*, vol. 54, pp. 303–322, 2021.

[7] M. Mirmehdi, *Handbook of texture analysis*, Imperial College Press, 2008.

[8] R. Lopes, A. Ayache, N. Makni, P. Puech, A. Villers, S. Mordon, and N. Betrouni, "Prostate cancer characterization on mr images using fractal features," *Medical physics*, vol. 38, no. 1, pp. 83–95, 2011.

[9] P. Abry, S. Jaffard, and H. Wendt, "When Van Gogh meets Mandelbrot: Multifractal classification of painting's texture," *Signal Process.*, vol. 93, no. 3, pp. 554–572, 2013.

[10] Z. Marin, K. A. Batchelder, B. C. Toner, L. Guimond, E. Gerasimova-Chechkina, A. R. Harrow, A. Arneodo, and A. Khalil, "Mammographic evidence of microenvironment changes in tumorous breasts," *Medical Physics*, vol. 44, no. 4, pp. 1324–1336, 2017.

[11] F.J.P Richard, "Analysis of anisotropic brownian textures and application to lesion detection in mammograms," *Procedia Environmental Sciences*, vol. 27, pp. 16–20, 2015.

[12] F.J.P. Richard, "Anisotropy of hölder gaussian random fields: characterization, estimation, and application to image textures," *Statistics and Computing*, vol. 28, no. 6, pp. 1155–1168, 2018.

[13] B. Pascal, N. Pustelnik, P. Abry, J.-C. Géminard, and V. Vidal, "Parameter-free and fast nonlinear piecewise filtering. Application to experimental physics," *Annals of Telecommunications*, vol. 75, pp. 655–671, 2020.

[14] V. Andrearczyk and P.F. Whelan, "Texture segmentation with Fully Convolutional Networks," *arXiv:1703.05230*, 2017.

[15] N. Pustelnik, H. Wendt, P. Abry, and N. Dobigeon, "Combining local regularity estimation and total variation optimization for scale-free texture segmentation," *IEEE Trans. Comput. Imaging*, vol. 2, no. 4, pp. 468–479, 2016.

[16] A. Bonami and A. Estrade, "Anisotropic analysis of some gaussian models," *Journal of Fourier analysis and applications*, vol. 9, no. 3, pp. 215–236, 2003.

[17] H. Biermé, "Introduction to random fields and scale invariance," *Stochastic Geometry: Modern Research Frontiers*, pp. 129–180, 2019.

[18] M. Clausel and B. Vedel, "Explicit construction of operator scaling gaussian random fields," *Fractals*, vol. 19, no. 01, pp. 101–111, 2011.

[19] K. Polisano, M. Clausel, V. Perrier, and L. Condat, "Texture modeling by gaussian fields with prescribed local orientation," in *2014 IEEE International Conference on Image Processing (ICIP)*, Paris, France, 2014, pp. 6091–6095.

[20] F. Richard and H. Bierme, "Statistical tests of anisotropy for fractional brownian textures. application to full-field digital mammography," *J. Math. Imag. Vis.*, vol. 36, no. 3, pp. 227–240, 2010.

[21] K. Polisano, *Modélisation de textures anisotropes par la transformée en ondelettes monogéniques*, Ph.D. thesis, Université Grenoble Alpes, 2017.

[22] H. Wendt, S. G. Roux, S. Jaffard, and P. Abry, "Wavelet leaders and bootstrap for multifractal analysis of images," *Signal Processing*, vol. 89, no. 6, pp. 1100–1114, 2009.

[23] I.W. Selesnick, R.G. Baraniuk, and N.C. Kingsbury, "The Dual-Tree Complex wavelet transform," *IEEE Signal Processing Magazine*, vol. 22, no. 6, pp. 123–151, 2005.

[24] N. C. Kingsbury, "Rotation-invariant local feature matching with complex wavelets," in *In Proc. EUSIPCO*, Florence, Italy, Sept. 4-8, 2006.

[25] J. D. B. Nelson and N. C. Kingsbury, "Dual-Tree wavelets for estimation of locally varying and anisotropic fractal dimension," in *Proc. Int. Conf. Image Process*, Hong Kong, Sept. 26-29, 2010.

[26] S. Mallat, "A wavelet tour of signal processing," 1999.

[27] I.W. Selesnick and I. Bayram, "On the Dual-Tree Complex wavelet packet and M-band transforms," *IEEE Trans. Signal Process.*, vol. 56, no. 6, pp. 2298–2310, 2008.

[28] P. Abry, D. Veitch, and P. Flandrin, "Long-range dependence: Revisiting aggregation with wavelets," *Journal of Time Series Analysis*, vol. 19, no. 3, pp. 253–266, 1998.

[29] B. Whitcher, P. Guttorp, and D. B Percival, "Wavelet analysis of covariance with application to atmospheric time series," *Journal of Geophysical Research: Atmospheres*, vol. 105, no. D11, pp. 14941–14962, 2000.

[30] P. Abry and G. Didier, "Wavelet estimation for operator fractional brownian motion," *Bernoulli*, vol. 24, no. 2, pp. 895–928, 2018.

[31] A. Ayache, A. Bonami, and A. Estrade, "Identification and series decomposition of anisotropic gaussian fields," in *More Progresses In Analysis*, pp. 441–450. World Scientific, 2009.

[32] D. Veitch and P. Abry, "A wavelet-based joint estimator of the parameters of long-range dependence," *IEEE Trans. Inform. Theory*, vol. 45, no. 3, pp. 878–897, 1999.

[33] P. L. Combettes and J.-C. Pesquet, "Proximal splitting methods in signal processing," in *Fixed-Point Algorithms for Inverse Problems in Science and Engineering*, H. H. Bauschke, R. S. Burachik, P. L. Combettes, V. Elser, D. R. Luke, and H. Wolkowicz, Eds., pp. 185–212. Springer-Verlag, New York, 2011.

[34] A. Chambolle and T. Pock, "A first-order primal-dual algorithm for convex problems with applications to imaging," *J. Math. Imag. Vis.*, vol. 40, no. 1, pp. 120–145, 2011.

[35] N. Parikh and S. Boyd, "Proximal algorithms," *Foundations and Trends in Optimization*, vol. 1, no. 3, pp. 123–231, 2014.